

MIT Open Access Articles

Implanted Nanosensors in Marine Organisms for Physiological Biologging: Design, Feasibility, and Species Variability

The MIT Faculty has made this article openly available. **Please share**
how this access benefits you. Your story matters.

As Published: 10.1021/ACSENSORS.8B00538

Publisher: American Chemical Society (ACS)

Persistent URL: <https://hdl.handle.net/1721.1/134899>

Version: Author's final manuscript: final author's manuscript post peer review, without publisher's formatting or copy editing

Terms of Use: Article is made available in accordance with the publisher's policy and may be subject to US copyright law. Please refer to the publisher's site for terms of use.



1 Implanted Nanosensors in Marine Organisms for Physiological 2 Biologging: Design, Feasibility, and Species Variability

3 Michael A. Lee,[†] Freddy T. Nguyen,[†] Kathleen Scott,[‡] Nathan Y.L. Chan,[§] Naveed Ali Bakh,[†]
4 Kelvin K. Jones,[†] Crystal Pham,[†] Pablo Garcia-Salinas,^{||} Daniel Garcia-Parraga,^{||} Andreas Fahlman,^{||}
5 Vicente Marco,^{||} Volodymyr B. Koman,[†] Ronnie J. Oliver,[†] Lloyd W. Hopkins,[⊥] Consuelo Rubio,^{||}
6 Rory P. Wilson,[⊥] Mark G. Meekan,[#] Carlos M. Duarte,[¶] and Michael S. Strano^{*,†,Ⓛ}

7 [†]Department of Chemical Engineering and [§]Division of Comparative Medicine, Massachusetts Institute of Technology, Cambridge,
8 Massachusetts 02139, United States

9 [‡]Office of Animal Resources, University of Iowa, Iowa City, Iowa 52242, United States

10 ^{||}Fundación Oceanogràfic de la Comunitat Valenciana, Research Department, Ciudad de las Artes y las Ciencias, 46013 Valencia,
11 Spain

12 [⊥]Biosciences, College of Science, Swansea University, Singleton Park, Swansea SA2 8PP, United Kingdom

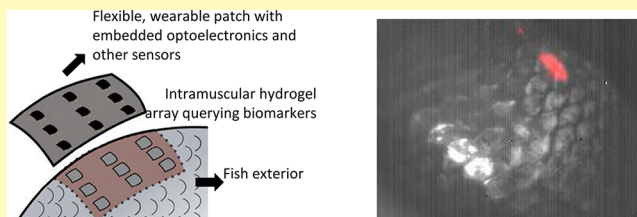
13 [#]Australian Institute of Marine Science, the Indian Ocean Marine Research Centre (IOMRC), University of Western Australia
14 Oceans Institute, 35 Stirling Highway, Crawley, Western Australia 6009, Australia

15 [¶]Red Sea Research Center, Division of Biological and Environmental Sciences and Engineering, King Abdullah University of Science
16 and Technology, Thuwal 23955-6900, Saudi Arabia

17 **S** Supporting Information

18 **ABSTRACT:** In recent decades, biologists have sought to tag
19 animals with various sensors to study aspects of their behavior
20 otherwise inaccessible from controlled laboratory experiments.
21 Despite this, chemical information, both environmental and
22 physiological, remains challenging to collect despite its
23 tremendous potential to elucidate a wide range of animal
24 behaviors. In this work, we explore the design, feasibility, and
25 data collection constraints of implantable, near-infrared fluo-
26 rescent nanosensors based on DNA-wrapped single-wall carbon nanotubes (SWNT) embedded within a biocompatible poly(ethylene
27 glycol) diacrylate (PEGDA) hydrogel. These sensors are enabled by Corona Phase Molecular Recognition (CoPhMoRe) to provide
28 selective chemical detection for marine organism biologging. Riboflavin, a key nutrient in oxidative phosphorylation, is utilized as a
29 model analyte in *in vitro* and *ex vivo* tissue measurements. Nine species of bony fish, sharks, eels, and turtles were utilized on site at
30 Oceanogràfic in Valencia, Spain to investigate sensor design parameters, including implantation depth, sensor imaging and detection
31 limits, fluence, and stability, as well as acute and long-term biocompatibility. Hydrogels were implanted subcutaneously and imaged
32 using a customized, field-portable Raspberry Pi camera system. Hydrogels could be detected up to depths of 7 mm in the skin and
33 muscle tissue of deceased teleost fish (*Sparus aurata* and *Stenotomus chrysops*) and a deceased catshark (*Galeus melastomus*). The
34 effects of tissue heterogeneity on hydrogel delivery and fluorescence visibility were explored, with darker tissues masking hydrogel
35 fluorescence. Hydrogels were implanted into a living eastern river cooter (*Pseudemys concinna*), a European eel (*Anguilla anguilla*), and
36 a second species of catshark (*Scyliorhinus stellaris*). The animals displayed no observable changes in movement and feeding patterns.
37 Imaging by high-resolution ultrasound indicated no changes in tissue structure in the eel and catshark. In the turtle, some tissue
38 reaction was detected upon dissection and histopathology. Analysis of movement patterns in sarasa comet goldfish (*Carassius auratus*)
39 indicated that the hydrogel implants did not affect swimming patterns. Taken together, these results indicate that this implantable form
40 factor is a promising technique for biologging using aquatic vertebrates with further development. Future work will tune the sensor
41 detection range to the physiological range of riboflavin, develop strategies to normalize sensor signal to account for the optical
42 heterogeneity of animal tissues, and design a flexible, wearable device incorporating optoelectronic components that will enable sensor
43 measurements in moving animals. This work advances the application of nanosensors to organisms beyond the commonly used rodent
44 and zebrafish models and is an important step toward the physiological biologging of aquatic organisms.

45 **KEYWORDS:** SWNT, *in vivo*, biologging, aquatic organisms, hydrogel, sensor



46 **I**n recent decades, the biologging community has attached
47 various types of sensors to animals to characterize animal
48 behavior in the context of their environments.¹ These studies

Received: June 22, 2018

Accepted: November 20, 2018

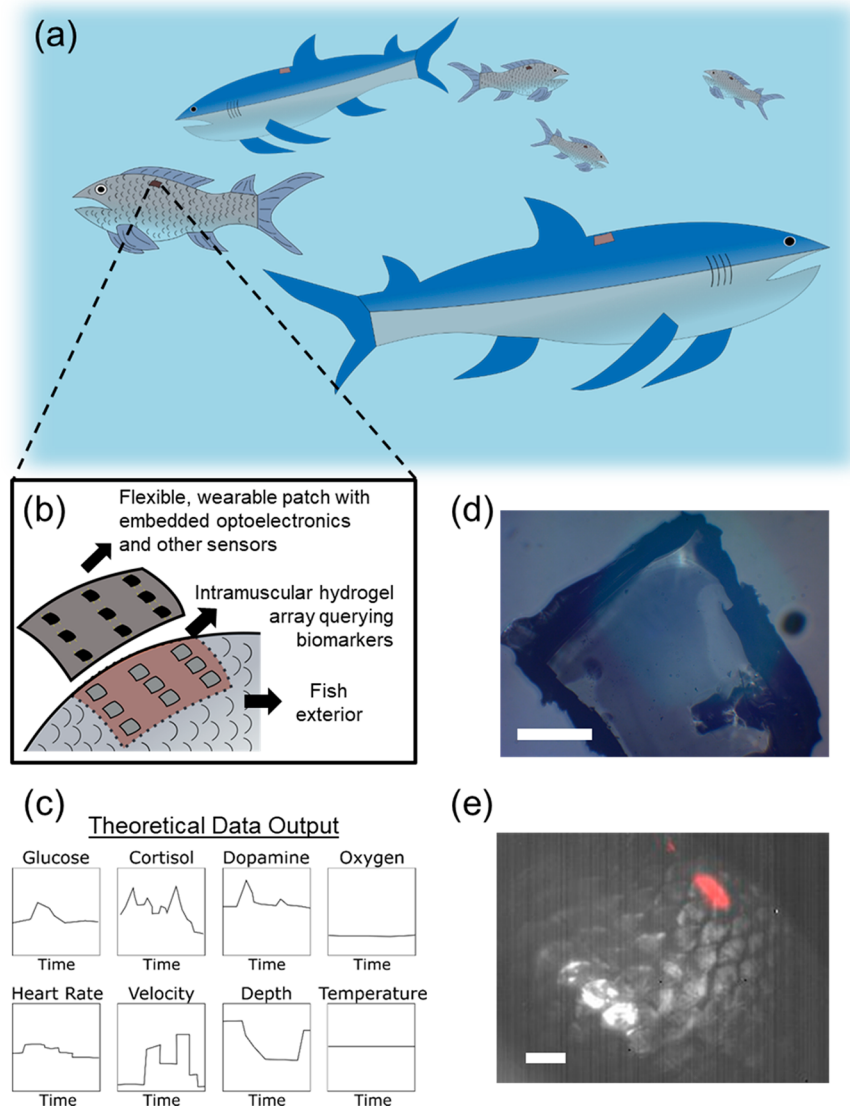


Figure 1. Vision for the future application of CoPhMoRe sensors to physiological biologging of marine organisms. (a) Animals of various sizes and ecological niches tagged with minimally invasive sensors collecting multivariate data sets continuously. (b) Theoretical design of a future biologging system. Hydrogel implants, encapsulating nanoparticles engineered to modulate their fluorescence in response to the local concentration of specific bioanalytes, are injected at a fixed depth in the intramuscular space, where they query biological fluid. Atop the fish's exterior is a flexible, wearable patch that contains embedded optoelectronics to excite and collect hydrogel fluorescence. The elastomer protects the electronic components from the surrounding aquatic environment, as well as conforming to the animal's movements. The device also incorporates other sensors to track animal movement and environmental conditions. The work herein describes the development of the hydrogel component of this theoretical device. (c) Theoretical data output of envisioned device. The device collects biochemical information and other animal-derived and environmental parameters such as velocity, depth, temperature, etc. (d) Visible image of SWNT-gels (scale = 0.5 mm). (e) Overlay of bright field image of sarasa comet goldfish (*Carassius auratus*) and fluorescence image of implanted hydrogel (scale = 10 mm).

49 have produced key insights into a wide range of ecological
 50 phenomena, including the metabolic energy balance,² preda-
 51 tor–prey relationships,³ the ecological effects of climate
 52 change,⁴ the impact of human activity on animals,⁵ and other
 53 behaviors related to feeding,⁶ migration,⁷ and reproduction.⁸
 54 However, deployed sensors have largely been limited to
 55 environmental parameter sensors (temperature, pressure, and
 56 salinity), movement and location sensors (accelerometers and
 57 GPS), and vital sign sensors, such as heart rate monitors.²
 58 Notably missing from these tools are chemical sensors. These
 59 may be outward-facing, measuring analytes in the local
 60 environment around the animal, or inward-facing, measuring
 61 biochemical signaling pathways within the animal. The advent of
 62 novel technologies capable of real-time, continuous chemical

sensing, such as those enabled by Corona Phase Molecular
 63 Recognition (CoPhMoRe), may enable access to this
 64 information and thereby significantly advance biologging
 65 studies.⁹ Herein, we explore, for the first time, several design
 66 and operation issues associated with implantable sensors of this
 67 type for biologging applications, using near-infrared (nIR)
 68 fluorescent carbon nanotube sensors as a model for marine
 69 organisms to address aspects of feasibility. For this study and
 70 purpose, we have assembled a unique team of marine biologists,
 71 sensor developers, and engineers to address this challenge, as
 72 coauthors of this study. 73

Recent developments in *in vivo* sensing technologies offer
 74 tremendous opportunities for biologists to probe the chemical
 75 network underpinning animal behaviors. As many excellent
 76

77 reviews have reported, *in vivo* sensors operating in several
78 modalities—including optical and electrochemical—have been
79 developed to measure a variety of biomarkers, including ions,
80 reactive oxygen species, redox active molecules, oxygen, metals,
81 and macromolecules, among many others.^{10–18} Recently, Sun et
82 al. measured glucose in mice using oxygen-sensitive polymer
83 dots and a smartphone.¹⁹ Measurements of hypochlorous acid
84 and pH have been performed in zebrafish and their embryos.^{20,21}
85 Ferreira et al. modified carbon fiber microelectrodes and
86 simultaneously measured ascorbate and glutamate in the
87 hippocampi of anesthetized rats.²² Despite these advances, the
88 continuous glucose monitor remains one of the few technologies
89 to be adopted due to stringent analytical and biocompatibility
90 requirements for sensor integrity in *in vivo* environments.^{13,14}
91 Although biologically derived units such as antibodies, aptamers,
92 and enzymes have traditionally been used for chemical
93 sensing,²³ they may lose their capability for molecular
94 recognition when conjugated to other sensor components and
95 may also suffer from limited thermal and chemical stability,
96 restricting their use *in vivo* to short periods of time.²⁴
97 Synthetic sensing approaches have overcome some of these
98 disadvantages. Our group has developed Corona Phase
99 Molecular Recognition (CoPhMoRe), which uses a nIR
100 fluorescent nanoparticle that acts as both the molecular
101 recognition unit and the reporter of binding events.⁹ An
102 amphiphilic polymer or surfactant adsorbs onto singly dispersed
103 single-wall carbon nanotubes (SWNT) via hydrophobic
104 interactions. The hydrophilic groups on the polymer provide
105 the dispersion colloidal stability in aqueous solutions, where a
106 majority of bioanalytes exist. The conformation of the adsorbed
107 phase, or the corona, modulates analyte binding to the
108 nanoparticle and provides selectivity. Upon analyte binding,
109 the fluorescence intensity and/or peak wavelength may change.
110 To date, CoPhMoRe sensors have been fabricated for a variety
111 of molecules, including nitric oxide,²⁵ hydrogen peroxide,²⁶
112 riboflavin, L-thyroxine, estradiol,⁹ dopamine,^{27,28} fibrinogen,²⁴
113 and insulin.²⁹ The nitric oxide sensor has been demonstrated *in*
114 *vivo* and shown to have a fluorescence stability of over 400 days
115 within the body of a mouse.³⁰
116 The challenge facing researchers is to now incorporate these
117 new types of physiological sensors into biologging devices.³¹ In
118 the past, the biologging community has traditionally focused on
119 sensors that describe the behaviors, external environments, and
120 location of animals. Accelerometers, depth, and temperature
121 sensors and Argos satellite-linked and GPS tags have been
122 central to this task.³² For example, using accelerometers, Wilson
123 et al. studied the significance of neck length in swimming and
124 foraging behaviors in Imperial cormorants and Megallanic
125 penguins.³³ Hays et al. used records from satellite tagging of
126 thousands of sea turtles to compare their migration distances
127 with those of other similarly sized marine animals,⁷ and Meekan
128 et al. used a combination of an accelerometer, magnetometer,
129 GPS, and depth sensors to study the energy efficiency of whale
130 shark movement patterns.³⁴
131 The combination of sensors that collect data sets of
132 movement, location, and relevant biochemical parameters
133 (such as glucose, dopamine, and cortisol)^{28,29,35} into biologging
134 tags potentially offers unprecedented insights into the behavior,
135 ecology, and condition of animals. To date, physiological data in
136 biologging tags has mostly been obtained from electromyogram
137 (EMG) and heart rate sensors.² Although there have been a few
138 examples of bioanalyte measurements in extracted blood,^{36–38}
139 the measurement of biomarkers in sampled fluid *ex vivo* offers

limited information and may introduce artifacts due to the
capture and restraint of the animal.³⁵ CoPhMoRe sensors
incorporated into animal-borne sensor tags have the potential to
transform biologging studies by giving researchers continuous
and real-time access to biomarkers reflecting the condition of
free-living animals (Figure 1).^{39,40}

In this work, as a model sensor implant, we use DNA-wrapped
SWNT that we have fabricated and encapsulated into a
biocompatible poly(ethylene glycol diacrylate) (PEGDA)
hydrogel and calibrated against riboflavin, an essential nutrient
involved in oxidative phosphorylation.⁴¹ *In vitro* characterization
and experiments with two species of marine organisms were
performed at MIT, whereas experiments with an additional
seven species were performed at Oceanogràfic in Valencia, Spain
from January 30 to February 1, 2018. The implants were
delivered via trocar to both recently deceased and living animals.
The hydrogel detection limit with injection depth was
determined, and the effects of tissue heterogeneity on
fluorescence detection were explored. The three living animals
showed no external signs of adverse health or behavioral changes
one month after implantation. However, in the case of the turtle,
some tissue reaction was detected upon dissection and
histopathology. At MIT, analysis of goldfish swimming patterns
indicated that the hydrogel implants do not impair animal
movement. All together, these data indicate the feasibility of
using CoPhMoRe sensors for marine organism biologging with
further improvements to sensor detection limits, normalization
of sensor signal to account for individual tissue optical
properties, and wearable fluorescence device design.

METHODS AND MATERIALS

Materials. (6,5)-Enriched SWNTs produced by the CoMoCAT
process (lot # MKBZ1159 V) were purchased from Sigma-Aldrich.
Single-stranded (AC)₁₅ was purchased from Integrated DNA
Technologies, while PEGDA ($M_n = 8000$) was purchased from Alfa
Aesar. Unless otherwise noted, other reagents were purchased from
Sigma-Aldrich.

Sensor Fabrication. SWNT (1 mg/mL) and ss(AC)₁₅ (2 mg/mL)
were mixed in 2 mL of 100 mM sodium chloride. The mixture was bath
sonicated for 10 min, followed by sonication with a 3 mm probe at 4 W
for 20 min (QSonica). The suspension was centrifuged at 32,000 rcf for
3 h, and the top 80% of the supernatant was collected for further use.
Free DNA was removed using 100 kDa MWCO centrifugal filters
(Merck Millipore) with 5 volumetric replacements with 1× phosphate
buffered saline (PBS). UV–vis–NIR absorption spectra were collected
to verify successful suspension. The SWNT mass concentration was
calculated using the absorption value at 632 nm.

ssDNA-SWNT (0.1 mg/mL), PEGDA (100 mg/mL), and 2-
hydroxy-4'-(2-hydroxyethoxy)-2-methylpropiophenone (0.175 mg/
mL) were mixed in 1× PBS, cast into glass molds, and incubated for
30 min under a nitrogen atmosphere. The samples were then
illuminated under 365 nm ultraviolet radiation (UVP Blak-Ray XX-
15BLB, 15 W) for 60 min. The hydrogels were removed from the molds
and incubated in excess 1× PBS for 48 h to remove unreacted
monomers and unencapsulated SWNT. The hydrogels were then
incubated in fresh 1× PBS until further use.

In Vitro Characterization. UV–vis–NIR absorption spectra were
measured for both solution phase and hydrogel encapsulated ssDNA-
SWNT (Shimadzu UV-3101PC). Fluorescence spectra were measured
in a custom-built NIR microscope. Samples were illuminated using a
785 nm photodiode laser (B&W Tek. Inc.) and imaged using a Zeiss
AxioVision inverted microscope with appropriate optical filters. The
fluorescence was passed through a Princeton Instruments Acton
SP2500 spectrometer and measured using a liquid nitrogen cooled
Princeton Instruments InGaAs 1D detector.

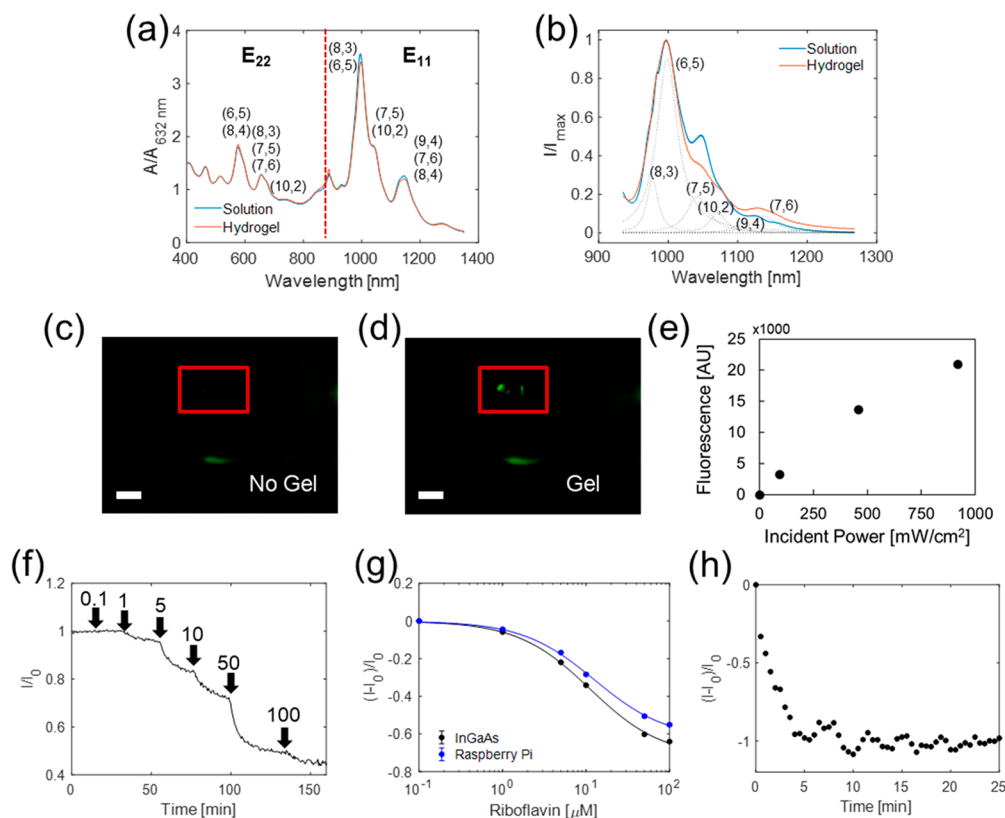


Figure 2. *In vitro* and *ex vivo* sensor characterization. (a) Normalized UV–vis–NIR absorption spectra and (b) fluorescence emission spectrum at 785 nm excitation of ss(AC)₁₅-wrapped (6,5) CoMoCAT SWNT. Spectra were measured for solution phase SWNT and SWNT-gels. The absorption spectrum shows both the excitation (E_{22}) and fluorescence emission peaks (E_{11}) for the corresponding SWNT chiralities given in parentheses. The fluorescence spectrum was decomposed into individual peaks corresponding to the labeled SWNT chiralities. (c,d) Images taken with Raspberry Pi imaging setup (c) without and (d) with a SWNT-gel. (e) Hydrogel fluorescence increased with larger incident excitation power. (f) Fluorescence decreased with stepwise increases in riboflavin concentration between 1 to 100 μM , as measured by a Raspberry Pi camera. (g) Riboflavin calibration curves obtained with an InGaAs camera and the Raspberry Pi camera show good agreement. (h) SWNT-gel response to bolus injection of 100 μM riboflavin while placed 1 mm deep into *ex vivo* tissue sample of *Stenotomus chrysops*. The fluorescence decreased below the limit of detection of the Raspberry Pi camera.

204 Riboflavin was used as a model analyte to test hydrogel chemical
205 sensitivity *in vitro* and *ex vivo*. Hydrogels were cut into $5 \times 5 \times 1 \text{ mm}^3$
206 sections and placed inside perfusion channels (ibidi μ -Slide III 3D
207 Perfusion). Hydrogel fluorescence was monitored while varying the
208 concentration of riboflavin in $1 \times \text{PBS}$ between 0–100 μM at a flow rate
209 of 0.3 mL/min. Fluorescence images were taken using a liquid nitrogen
210 cooled Princeton Instruments InGaAs 2D detector. These measure-
211 ments were also performed on a $5 \times 5 \times 2 \text{ mm}^3$ section of hydrogel
212 placed 1 mm below the surface of skin and muscle tissue of *Stenotomus*
213 *chrysops*. A 500 μL bolus of 100 μM riboflavin was introduced atop of
214 the hydrogel.

215 ***In Vivo* Implantation.** All procedures described below were
216 approved by the animal ethics committee of the Fundaci3n Ocean-
217 ografic de la Comunitat Valenciana and performed at Oceanogr3fic over
218 the duration of the experiments.

219 Prior to implantation, hydrogels were illuminated by UV light for 15
220 min and handled in a biological hood (Telstar AV-100) thereafter to
221 ensure sterility. Hydrogels were cut to a $1 \times 5 \times 1 \text{ mm}^3$ block and loaded
222 into 12 gauge transponder needles from which the microchips were
223 removed (Avid Suds Monoject).

224 The implantation procedure varied depending on the target
225 organism. In the case of deceased animals, all animals were injected
226 without further treatment of the skin. Hydrogels were placed at the
227 desired location and penetration depth by using the needle length and
228 angle of insertion as a guide.

229 A live European eel (*Anguilla anguilla*) was anesthetized prior to
230 injection by submersion in a 70 mg/L benzocaine solution. When the
231 eel was nonresponsive, the injection site on the dorsal side was washed

with sterile saline, and the hydrogel was injected. The eel was moved to
new water and allowed to recover prior to further handling.

232
233
234 A live eastern river cooter (*Pseudemys concinna*) and catshark (
Scyliorhinus stellaris) were restrained by animal care personnel for
235 hydrogel implantations. The skin of the shark was washed with sterile
236 saline, whereas the skin of the turtle was disinfected with iodopovidone.
237 The hydrogel was injected subcutaneously in the dorsal area of the
238 shark at the level of the second dorsal fin and in the dorsal part of the
239 cranial tram of the turtle's neck.
240

241 After implantation, the animals were monitored for 2 months to
242 determine tolerance to the implants and changes in swimming and
243 feeding behavior. High-resolution ultrasound images of the implanta-
244 tion site were used to noninvasively study the impacts of implantation
245 on tissues. After one month, the turtle was euthanized (for reasons not
246 related to this study), allowing biopsies of the implantation site to be
247 collected for histopathology.

248 **Imaging Using Raspberry Pi.** The imaging system consisted of a
249 Raspberry Pi 3 (Adafruit) with a 5 MP camera with the IR filter
250 removed (SainSmart). The camera was placed inside of a 1 in. lens tube.
251 The camera was used without further modification when taking
252 brightfield images. The Picamera software package was used to control
253 the camera.

254 When taking fluorescence images, the hydrogels were illuminated
255 with a 200 mW 561 nm laser (Opto Engine LLC) passing through a
256 collimator. Fluorescence passed through a 900 long-pass filter prior to
257 collection by the camera. Fluorescence was quantified by taking two
258 images before and after hydrogel placement and calculating the
259 difference in gray value in the region of interest. For all images, the

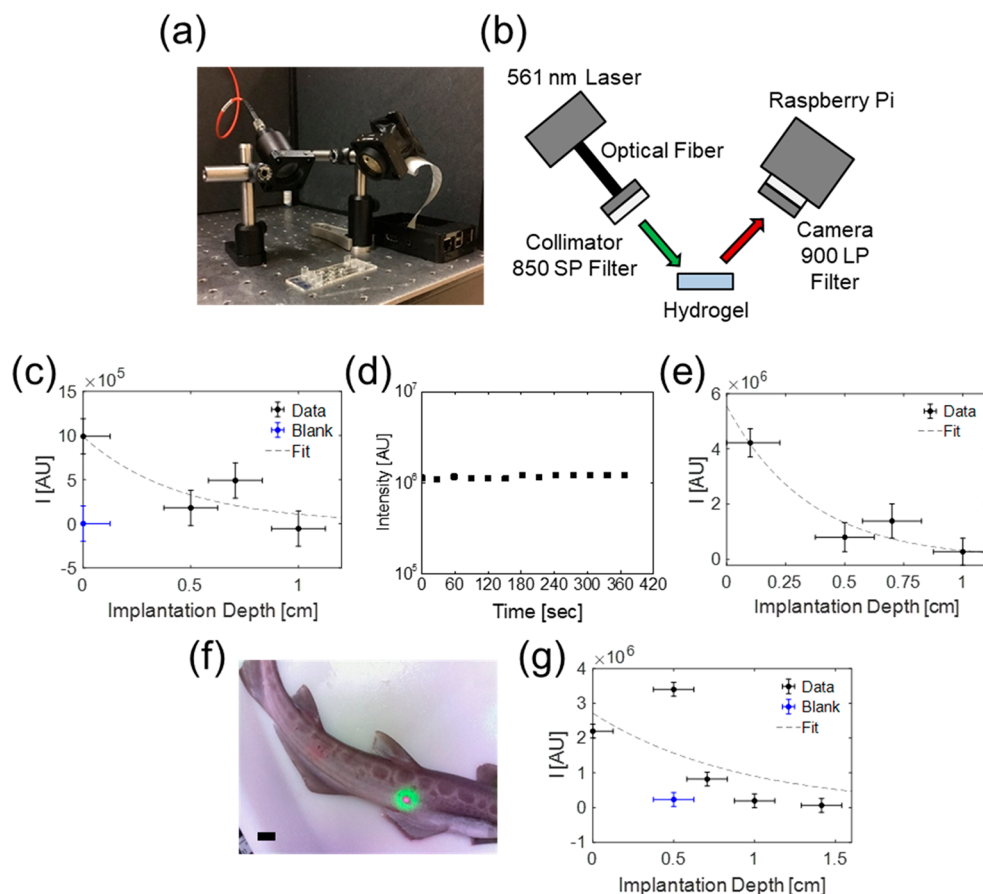


Figure 3. Effect of hydrogel implantation depth on fluorescence detection in teleosts (*Sparus aurata* and *Stenotomus chrysops*) and cat shark (*Galeus melastomus*). (a,b) Imaging setup and schematic. A fiber-coupled 561 nm laser fitted with an 850 short-pass filter was used to illuminate the implantation site before and after intramuscular delivery of hydrogels into previously deceased animals via trocar. The signal was collected by a Raspberry Pi camera connected to a 900 long-pass filter. The difference in gray values with and without the hydrogel was calculated. (c) In *Sparus aurata*, detectable hydrogel fluorescence decreased as injection depth was increased from just below the skin down to a limit of 0.7 cm. A nonfluorescent hydrogel was injected just superficially below the skin and imaged to give the threshold difference in intensity for the signal to be attributable to the hydrogel and not to other artifacts, such as movement of the fish relative to the laser. (d) A superficially implanted SWNT-gel in *Sparus aurata* exhibited a steady fluorescence signal when imaged over 6 min. (e) The detection limit of SWNT-gels in *Stenotomus chrysops* was 0.7 cm. (f) Overlay of brightfield and fluorescence images of a fluorescent hydrogel implanted 0.5 cm below the skin in *Galeus melastomus* [scale = 20 mm]. (g) SWNT-gels were detected down to a depth of 0.7 cm in *Galeus melastomus*, as compared to a nonfluorescent hydrogel implanted at a depth of 0.5 cm.

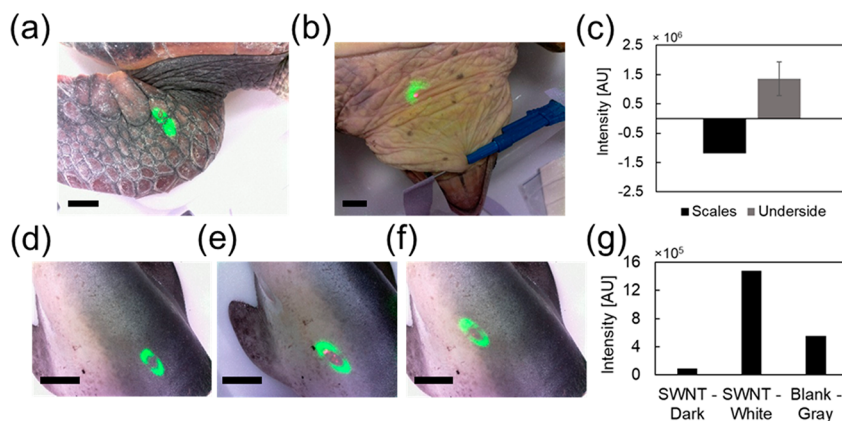


Figure 4. Detection of fluorescent hydrogels implanted superficially in optically heterogeneous tissues. Fluorescent hydrogels were implanted into (a) the scaly legs and (b) softer flesh beneath the neck of a sea turtle (*Caretta caretta*) (scale = 20 mm). (c) Hydrogel fluorescence was detected in the neck but not the scaly legs. SWNT-gels were implanted subcutaneously in (d) dark and (e) white regions of a blue shark (*Prionace glauca*). A nonfluorescent hydrogel was implanted in (f) gray region of the tissue. (g) Fluorescence could be detected underneath white skin but not dark skin. The blank hydrogel in the gray region provided a baseline against which to determine fluorescence detection. Scale in all images is 20 mm.

260 autowhite balance gains, exposure times, and shutter speed were set
261 manually. The analog and digital gains were kept constant by
262 equilibration of the camera for a 1 min period.

263 **Goldfish Hydrogel Implantations and Motion Tracking.** All
264 experimental details below and associated husbandry procedures were
265 reviewed and approved by the Committee on Animal Care at MIT.

266 Two sarasa comet goldfish (*Carassius auratus*) were purchased from
267 LiveAquaria, housed in a 110 L glass aquarium with dimensions of 76 ×
268 42 × 30 cm³ (length × width × height), and allowed to acclimate for at
269 least 2 weeks prior to experimental manipulation. The water was
270 maintained at 24 °C, and the aquarium was lit daily for 10 h. Fish were
271 fed daily with flake foods (TetraFin).

272 Prior to implantation, hydrogels were treated under UV light for 15
273 min and handled in a biological hood thereafter to ensure sterility.
274 Hydrogels were cut to a 1 × 3 × 1 mm³ shape and loaded into 16 gauge
275 needles. Fish were anesthetized in a solution of 60 mg/L tricaine
276 methanesulfonate. When the fish were nonresponsive to handling and a
277 fin pinch, the hydrogels were injected into muscle just below the dorsal
278 fin. The fish were allowed to recover in a holding tank before being
279 returned to the home tank.

280 To determine the impact of the hydrogel implant on the animal's
281 health, its movements were recorded using a surveillance system
282 consisting of the Raspberry Pi 2 computer with a Raspberry Pi Camera
283 Board v 2. Fish movements were extracted using the Kinovea software.

284 After the experimental lifetime, the fish were euthanized by
285 submersion into a 500 mg/L solution of tricaine methanesulfonate.

286 ■ RESULTS AND DISCUSSION

287 **Sensor Fabrication and *in Vitro* Optical Character-**
288 **ization.** DNA-wrapped SWNT have been utilized in many
289 studies due to their high wrapping efficiency^{42,43} and flexibility
290 in selective sensing of different analytes.^{25–27,30,44} The UV–vis–
291 NIR absorption spectrum (Figure 2a) shows distinct peaks,
292 indicating successful nanoparticle suspension. Mass concen-
293 tration of total carbon in the solution was estimated using an
294 extinction coefficient of $\epsilon_{632\text{ nm}} = 0.036\text{ (mg/L)}^{-1}\text{ cm}^{-1}$.⁴⁵ Singly
295 dispersed ss(AC)₁₅-SWNT nanoparticles were produced at a
296 36% yield based on a carbon mass balance.

297 Peak position and relative peak intensities of ss(AC)₁₅-SWNT
298 in solution phase or encapsulated in the hydrogel (SWNT-gel)
299 were identical in both the absorption spectra and fluorescence
300 emission spectra (Figure 2b), indicating that the dielectric
301 environments surrounding the SWNT were nearly identical.^{46,47}
302 The absorption spectrum of the SWNT-gel indicated a final
303 concentration of 33 mg/L SWNT. However, the fluorescence
304 intensity of the SWNT-gel was only 50% of the intensity in the
305 equivalent concentration in solution phase. Sample geometry
306 contributed to this decrease, as the hydrogels are only 1 mm in
307 thickness, whereas liquid samples were typically 1 cm in height.
308 Additionally, the chemical environment of the sensors in the
309 hydrogel is different, in that the SWNT are diffusively
310 constrained by a polymer matrix. Free radicals that are generated
311 during the photopolymerization of the hydrogel may have also
312 chemically altered the DNA on the SWNT surface.

313 **Characterization of SWNT-Gel Pore Size.** The hydrogel
314 pore size formed by the spacing between cross-linked polymer
315 chains is a critical parameter that controls sensor functionality
316 and environment. The pores in the gel determine the size of the
317 analyte that is permitted to enter the network, as well as its rate
318 of diffusion, thereby affecting sensor response time.⁴⁸ The pore
319 size can also be used to exclude large molecular weight
320 interfering molecules to improve sensor selectivity. Further-
321 more, the hydrogel's pore diameter relative to nanoparticle size
322 dictates the degree of nanoparticle entrapment.⁴⁹

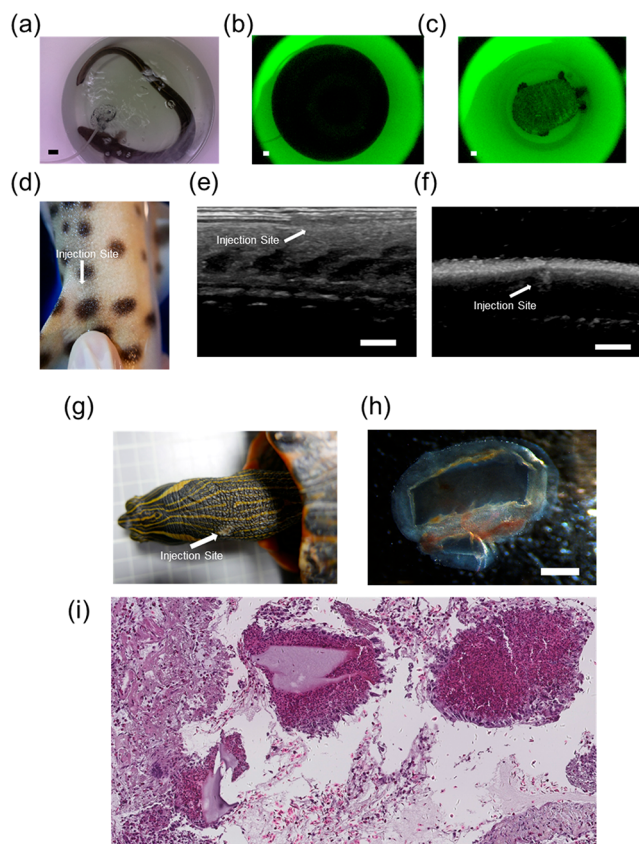


Figure 5. NIR fluorescent hydrogels implanted in a living European eel (*Anguilla anguilla*), eastern river cooter (*Pseudemmys concinna*), and catshark (*Scyliorhinus stellaris*). (a) Following implantation, attempts were made to track the fluorescence in the eel and turtle confined to a small space. (b,c) Dispersed laser excitation, animal movement, and long exposure times made these attempts unsuccessful in (b) the eel and (c) the turtle. All scalebars are 20 mm. (d) The implantation site fully healed in the catshark by 33 days post-implantation. (e,f) High resolution ultrasound images were taken to examine noninvasively tissue response to the implant 4 weeks after implantation in the (e) eel and (f) catshark (scale = 5 mm). The absence of significant changes in tissue architecture and echogenicity indicates that the hydrogels were well-tolerated in these organisms. (g) The injection site in the turtle did not heal completely 33 days post-implantation. (h) Hydrogels were removed from the turtle after 33 days and were found to be encapsulated by tissue. (i) Histology images from subcutaneous tissue surrounding the hydrogel implant in the turtle indicate a foreign body tissue reaction.

Swelling experiments were performed in 1× PBS to obtain the
average SWNT-gel pore size from the polymer network. The
swelling ratio was determined using the following equation

$$Q = \frac{m_{\text{swollen}}}{m_{\text{dry}}} = \alpha^{-1} \quad (1)$$

where Q is the hydrogel swelling ratio and m is the hydrogel
mass. Q can then be used to calculate the average pore
diameter:^{50,51}

$$\bar{M}_c^{-1} = \frac{2}{\bar{M}_n} - \frac{(\bar{v}/V_2)[\ln(1 - \alpha) + \alpha + \chi\alpha^2]}{\alpha^{1/3} - (2/\theta)\alpha} \quad (2)$$

$$\zeta = \alpha^{1/3} \left(\frac{2C_{\infty}I^2\bar{M}_c}{M_0} \right)^{1/2} \quad (3)$$

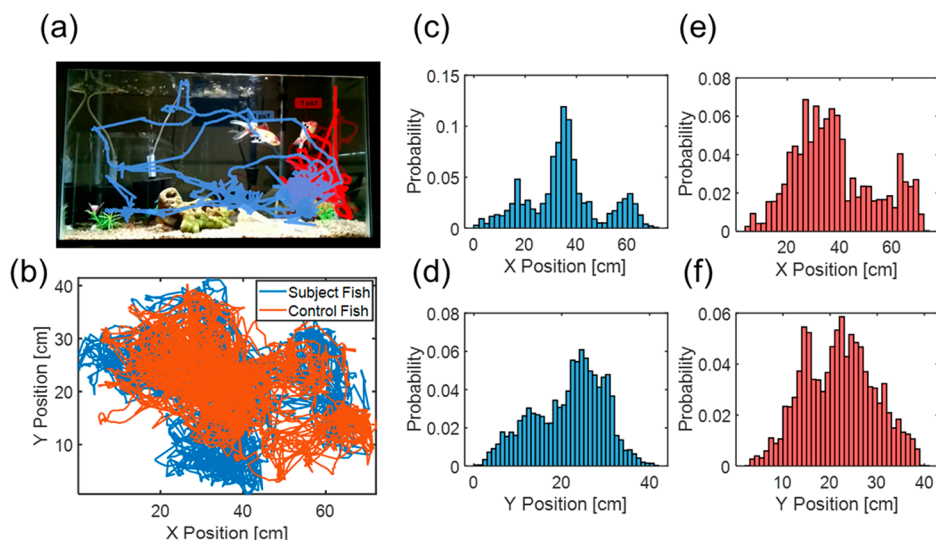


Figure 6. Quantification of hydrogel implant impact on animal health. (a) Snapshot of the capture video with corresponding sarasa comet goldfish (*Carassius auratus*) movement trajectories included. Blue corresponds to a fish in which a nIR fluorescent hydrogel was implanted, while orange corresponds to a control fish without a hydrogel implant. (b) Trajectories of fish taken for 1 h 2 days after a hydrogel was implanted into the subject fish. (c–f) X and Y position histograms for the subject fish (c,d) and control fish (e,f). The subject fish experienced neither impaired movement nor erratic movement due to the hydrogel implant, indicating good tolerance of the implant.

332 where \bar{M}_c is the molecular weight between cross-links, \bar{M}_n is the
 333 molecular weight of the polymers without cross-linking
 334 ($=8000$), \bar{v} is the specific volume of the polymer ($= 0.903$
 335 mL/g), V_2 is the specific volume of water ($= 18.01$ mL/mol), χ is
 336 the Flory–Huggins parameter ($= 0.3765$), θ is the functionality
 337 of PEGDA ($= 4$), ξ is the average mesh side, C_∞ is the Flory
 338 characteristic ratio ($= 6.9$), l is the carbon–carbon bond length
 339 ($= 0.154$ nm), and M_0 is the molar mass of the repeat unit ($=$
 340 44.05 g/mol). The Flory parameter was obtained from a
 341 previous study of PEG polymers.⁵² The average pore size was
 342 estimated to be 15 nm.

343 **Raspberry Pi Imaging Systems.** To understand the range
 344 of organism–environment interactions and document variation
 345 among individuals and populations, some biologging studies
 346 have deployed sensors on anywhere from dozens to hundreds of
 347 animals.^{7,53} To this end, some laboratory instruments are not
 348 practical due to their prohibitive cost for large-scale deployment,
 349 immobility, and fragility on a moving animal in its natural
 350 environment. For example, InGaAs cameras typically used to
 351 measure near-infrared fluorophores can weigh on the order of 5
 352 kg and can cost thousands of dollars.^{9,24,29} Consequently, we
 353 chose to use inexpensive and portable Raspberry Pi computers
 354 and cameras which cost on the order of tens of dollars. In the real
 355 application, the components of a Raspberry Pi imaging system
 356 can be readily incorporated into a miniaturized sensor suite.
 357 Recently, Göröcs et al. incorporated a similar CMOS image
 358 sensor into a portable imaging device weighing less than 40 g.³⁴

359 Because the optical sensors on the cameras are fabricated from
 360 silicon, which have limited sensitivity (<0.1 A/W above 980 nm)
 361 to the near-infrared fluorescence of SWNT (Figure S-1), we first
 362 verified that the hydrogels could be visualized by our system
 363 (Figure 2c,d). Analysis showed a linear trend of hydrogel
 364 fluorescence with incident laser power density (Figure 2e).

365 **Riboflavin as a Model Analyte for Chemical Sensing *in***
 366 ***Vitro* and *ex Vivo*.** Riboflavin plays a key role in the recycling of
 367 FADH and FAD⁺ in oxidative phosphorylation and is an
 368 essential nutrient in a fish's diet.^{41,55} Riboflavin exists in plasma
 369 typically between 1 and 100 nM.^{56,57} Furthermore, DNA

oligonucleotides of various sequences, when complexed to 370
 SWNTs, allow for a nIR fluorescence modulation in response to 371
 riboflavin binding via both intensity quenching and wavelength 372
 shifts,⁹ making it an ideal model analyte to evaluate *in vivo* 373
 sensing feasibility. 374

The SWNT-gels showed stepwise decreases in fluorescence 375
 with stepwise increases in surrounding riboflavin concentration, 376
 with sensitivity from 1 to 100 μ M (Figure 2f). The calibration 377
 curves were fitted to the following functional form: 378

$$\text{Response} = \frac{I - I_0}{I_0} = \beta \frac{C}{C + K_D} \quad (4) \quad 379$$

where β is the gain, C is the riboflavin concentration, and K_D is 380
 the equilibrium dissociation constant. To evaluate the perform- 381
 ance of the Raspberry Pi relative to typical laboratory 382
 equipment, we compared results obtained with a Princeton 383
 Instrument 2D InGaAs camera. The calibration curves showed 384
 good agreement (Figure 2g). For the InGaAs camera, β was 385
 -0.72 , and K_D was 11.3 μ M, while the corresponding values 386
 were -0.63 and 12.7 μ M for the Raspberry Pi. The difference in 387
 maximum response is a product of higher background signal in 388
 the Raspberry Pi, which partially masked the fluorescence 389
 quenching of the riboflavin. Future versions of the sensor tag will 390
 be designed to eliminate such interference by optimizing optical 391
 configurations and increase the sensitivity to detect physio- 392
 logical levels of riboflavin. 393

Furthermore, the fluorescence of the SWNT-gels decreased in 394
 response to a bolus of 100 μ M when placed in a 1-mm-thick skin 395
 and muscle tissue sample of *Stenotomus chrysops* (Figure 2h). 396
 The fluorescence decreased below the detection limit of the 397
 Raspberry Pi camera. 398

Optical Penetration Depth. We constructed a simplified, 399
 1-D mathematical model to describe the effects of material, 400
 tissue, and equipment properties on the optical signal from a 401
 sensor implanted into tissue. Incident excitation light is partially 402
 reflected from the epidermal interface 403

$$I_0 = I_i(1 - r_{\text{ex}}) \quad (5) \quad 404$$

where I_i and I_0 are the incident and transmitted excitation fluences, respectively, and r_{ex} is the epidermal reflectivity at the excitation wavelength. Tissue further attenuates excitation light according to the Beer–Lambert law

$$\log\left(\frac{I_0}{I}\right) = \gamma_{\text{ex}} d \quad (6)$$

where I is the fluence at the implantation site, γ_{ex} is the tissue extinction coefficient at the excitation wavelength, and d is distance through tissue. The fluorescence intensity of the hydrogel at the implantation site is described by

$$\log\left(1 - \frac{F_0}{\eta LA}\right) = -\epsilon_{\text{ex}} ct \quad (7)$$

where F_0 is the fluorescence intensity at the implantation site, η is the quantum efficiency of SWNT, A is the cross-sectional area of the hydrogel, ϵ_{ex} is the extinction coefficient of SWNT at the excitation wavelength, c is the concentration of SWNT in the hydrogel, and t is the hydrogel thickness. The thickness of the hydrogel is assumed to be negligible compared to the implantation depth. The fluorescence reaching the surface of the epidermis is given by the following equation

$$\log\left(\frac{F_0}{F}\right) = \gamma_{\text{em}} d \quad (8)$$

where F is the fluorescence reaching the epidermal interface, γ_{em} is the tissue extinction coefficient at the emission wavelength. Back-reflection of fluorescence may occur at the epidermal interface

$$F_f = F(1 - r_{\text{em}}) \quad (9)$$

where F_f is the fluorescence exiting the tissue and r_{em} is the reflectivity at the fluorescent wavelength. Assuming minimal scattering and absorption between the epidermal surface and the photodetector, the measured signal is described by

$$S = F_f R \quad (10)$$

where S is the signal, and R is the responsivity of the camera. Combining eqs 5–10 yields

$$\begin{aligned} \log\left(\frac{S}{\eta A R I_i (1 - r_{\text{ex}})(1 - r_{\text{em}})}\right) \\ = \log(1 - 10^{\epsilon_{\text{ex}} ct}) - d(\gamma_{\text{ex}} + \gamma_{\text{em}}) \end{aligned} \quad (11)$$

The terms in eq 11 can be classified into material, tissue, and equipment properties and tunable engineering parameters. The specific fluorophore dictates the value of η and ϵ_{ex} . Different tissues attenuate light transmission to varying extents and consequently have unique values of γ , which may be measured in a future study via light transmission measurements. Both absorption and scattering contribute to the extinction coefficient. Scattering decreases with increasing incident wavelength,⁵⁸ while absorption is largely determined by water and blood absorption, which is minimal in the SWNT fluorescent region.⁵⁹ Furthermore, unlike organic fluorophores, SWNT do not photobleach and thus exhibit a constant c as long as the implant maintains its integrity. Thus, the near-infrared fluorescence of SWNT is ideal for an *in vivo* optical biosensor due to the lack of photobleaching and the transparency of the near-infrared window.^{60,61} Controllable parameters include I_i , A , c , t , r , and d . Increased hydrogel thickness, fluorophore

concentration, equipment responsivity, and excitation power and decreased implantation depth increase the fluorescence signal. In a previous study, Iverson et al. measured the fluorescence of an alginate hydrogel with 10 mg/L SWNT to a depth of 5 mm in tissue phantoms using a hyperspectral CRI Maestro system.⁶²

For this application, consideration of the marine organism tissue properties is critical. Many fish species, including teleosts, have evolved skin containing significant amounts of reflective guanine crystals in the stratum argenteum and underneath the scales, which may camouflage the animal against predators. The reflective spectra of such biomaterials have been thoroughly characterized in previous work.⁶⁴ These different skin types will affect the penetration of light through tissue. Others, such as sharks and marine reptiles, have evolved thick, mechanically stiff skin and/or scales as protection against environmental hazards, which may require specialized methods of placing implantable devices.⁶⁵ All together, these factors suggest that each species should be considered individually when using implantable nIR fluorescent hydrogel sensors for biologging.

Two deceased teleosts (*Sparus aurata* and *Stenotomus chrysops*), a female adult catshark (*Galeus melastormus*) were used for the nIR penetration versus depth study. The teleosts were chosen because over 32,500 species exist, making them the largest category of vertebrates.⁶⁶ Furthermore, catsharks comprise over 10% of extant cartilaginous fish.⁶⁷ Images were taken of the fish before and after placement of the hydrogel using the Raspberry Pi camera system (Figure 3a,b). Movement of the animal relative to the imaging setup was minimized such that differences in signal between the two images is predominantly the hydrogel, not position change. In *Sparus aurata*, the nIR fluorescent SWNT-gels were detected up to a depth of 7 mm (Figure 3c). Injection of sham nonfluorescent hydrogels using the same method verified that the difference in signal due to movement was negligible compared to the additional signal from the fluorescence. The residual signal is a small change in laser reflection from a small shift in position of the fish tissue. The SWNT-gels also exhibited stable fluorescence (Figure 3d). This stability is critical, so that perturbations can be attributed solely to changes in analyte concentrations. For *Stenotomus chrysops* and *Galeus melastormus* (Figure 3e–g), the SWNT-gels were detected again to a depth of 7 mm over a minimum signal difference threshold determined by injection of a nonfluorescent hydrogel (Figure 3g). A simplified version of eq 11 was used to fit the data and reproduced the trends.

$$S = a \cdot 10^{b \cdot d + c} \quad (12)$$

The fit parameters are reported in Supporting Information.

As can be seen in Figure 3c,e,g, there was not a monotonic decrease in fluorescence with increasing depth. We attribute the noise to variations in hydrogel thickness, cross-sectional area, placement at the intended depth, and position relative to the excitation source. As illustrated by eq 11, variations in geometry and placement of the SWNT-gels necessarily change the signal by reducing the excitation power incident on the hydrogel and changing the attenuation distance of the excitation and fluorescence through tissue.

Although the penetration depth of the SWNT sensors in the target species were similar to that of previous studies,⁶² the maximum depth can be increased using several approaches. First, the excitation and fluorescence detection equipment can be optimized specifically for SWNT-based biosensors. An InGaAs photodetector, which has almost an order of magnitude

516 higher photoresponsivity (0.67 A/W at 1000 nm) may replace
517 the silicon-based camera (0.067 A/W at 1000 nm) used in this
518 study (Figure S-1). This equipment, along with other optical
519 components such as lenses, can be attached directly to the
520 animal instead of being placed at standoff distances, thus
521 reducing the optical path length, optimizing excitation and
522 fluorescence collection, and increasing signal. Alternatively,
523 optical fibers may be implanted transdermally, in the form of an
524 optode, to couple the excitation source directly with the
525 hydrogel and the hydrogel with the photodetector.⁶⁸

526 Ultimately, placement of the sensor could be influenced by
527 other factors in addition to optical penetration depth, including
528 local analyte concentration and sensor sensitivity. Many analytes
529 of interest, such as glucose, cortisol, and vitamins, exist in
530 interstitial fluids and can be theoretically queried with a hydrogel
531 implanted superficially atop the hypodermis.⁶⁹

532 **Tissue Heterogeneity.** Different color patterns of tissue
533 and mechanically distinct exteriors may exist on the skin of the
534 same animal, which may affect hydrogel implantation and/or
535 fluorescence visibility. To examine this issue, we implanted
536 hydrogels in different skin tissues of a juvenile female sea turtle (
537 *Caretta caretta*) and a juvenile male blue shark (*Prionace glauca*).
538 The sea turtle had both scaly and fleshy regions of the skin,⁶⁵
539 whereas the blue shark had distinctly colored regions ranging
540 from dark blue to white.⁷⁰

541 SWNT-gels were delivered in both the front right leg and the
542 flesh centered underneath the neck of the sea turtle (Figure
543 4a,b). As the needle could not pierce the scales, it was inserted
544 between them. The neck flesh was stretched prior to hydrogel
545 placement to prevent folding of additional skin on top of the
546 implant, avoiding artificial increases in the optical path length.
547 The hydrogel was not visible beneath the scales but was visible
548 beneath the fleshy skin of the neck (Figure 4c). SWNT-gel
549 sensors were placed underneath the white and dark sections of
550 shark's epidermis, and a nonfluorescent hydrogel was placed into
551 a gray area to provide a baseline against which nIR fluorescent
552 hydrogels could be compared (Figure 4d–f). The nIR
553 fluorescent hydrogel was visible beneath the white but not the
554 dark-colored epidermis (Figure 4g).

555 In both organisms, dark sections of tissue masked the nIR
556 fluorescence of the sensor implants. Increased melanin levels in
557 the epidermis result in higher absorption coefficients up to 1100
558 nm,^{71,72} resulting in less excitation of the hydrogel and
559 transmission of (6,5) SWNT fluorescence by increasing the
560 values of γ_{ex} and γ_{em} in eq 11. UV–vis–NIR absorption
561 measurements of tissue samples can quantify these wave-
562 length/tissue dependent effects in a future study.

563 These results indicate two additional requirements for nIR
564 fluorescent biosensors for *in vivo* applications. First, to maximize
565 the signal-to-noise ratio, sensors should be delivered to tissues
566 that are as optically transparent as possible for both the
567 excitation and emission wavelengths. Furthermore, sensor
568 fluorescence may have to be normalized against an invariant
569 internal standard to eliminate the effects of tissue hetero-
570 geneity.⁴⁴ Second, to deliver hydrogels via a minimally invasive
571 injection, some tissue sections will be inaccessible due to their
572 mechanical strength and rigidity.

573 **Imaging and Sensor Operation in Live Animals.** Several
574 questions regarding tolerance/biocompatibility of the implant
575 and its effects on behavior can only be answered using living
576 animals. A moving animal also adds greater complexity when
577 imaging which may require reconfigurations of the sensor.

A female adult European eel (*Anguilla anguilla*), a female adult 578
eastern river cooter (*Pseudemmys concinna*), and a juvenile male 579
catshark (*Scyliorhinus stellaris*) were tagged with sensor 580
hydrogels and monitored for up to 2 months. We attempted 581
to image the eel and turtle in a small bucket from a distance of 582
0.5 m, but were unsuccessful for several reasons (Figure 5a–c). 583
First, the camera and excitation sources were moved farther 584
away to image the entire field of view. This reduced both the 585
excitation power density incident upon the surface of the 586
epidermis from 150 to 0.3 mW/cm² and consequently the 587
fluorescence upon the camera's sensor by a factor of at least 500, 588
according to eq 11. Furthermore, the combination of a long 589
exposure time and animal movement apparently blurred the 590
images. 591

Engineering Design for nIR Fluorescent Hydrogel 592
Implants. A central goal of the current work is to utilize these 593
findings to design sensing hydrogel implants. A wearable 594
fluorescence reader that conforms to the animal's body as it 595
moves is necessary.⁷³ Fixing the position of the measurement 596
unit relative to the SWNT-gels eliminates changes in hydrogel 597
fluorescence due to a changing excitation field and/or 598
misalignment of the hydrogel and camera. Furthermore, placing 599
the measurement device directly on top of the hydrogel reduces 600
the optical path length, increasing the signal-to-noise ratio. As 601
such, the miniaturization into and attachment methods of a 602
flexible form factor are critical next steps. 603

Biocompatibility of the hydrogel was favorable in two of the 604
three animals. We found no changes in movement or feeding 605
behavior of the eel and catshark for two months post- 606
implantation (Figure 5d). In the ultrasound images, the 607
implantation site was identified via a slight change in tissue 608
structure and echogenicity, but the surrounding tissue was 609
completely normal (Figure 5e,f). In the case of a significant 610
foreign body reaction, larger changes in architecture and 611
echogenicity would be found in the periphery of the implant 612
as it becomes encapsulated.^{74,75} In contrast, histopathology 613
suggested that the turtle experienced some reaction to the 614
implant. The injection site did not heal cleanly (Figure 5g). It is 615
important to note that there may have been an infection of the 616
wound following implantation, precluding clean healing. 617
Granules containing hydrogel fragments were extracted from 618
the implantation site one month after the procedure (Figure 5h). 619
H&E stained tissue sections showed infiltration of inflammatory 620
cells into the deep dermis, hypodermis, and cutaneous muscle. 621
The infiltrate consisted of heterophiles, macrophages, and 622
several multinucleated giant cells, consistent with panniculitis 623
and a foreign body reaction to the implant (Figure 5i). However, 624
no behavioral changes were noted in the turtle. 625

A similar implantation procedure was performed on adult 626
Sarasa comet goldfish (*Carassius auratus*), and its movement 627
patterns were analyzed relative to a control goldfish without an 628
implant (Figure 6a). Animal trajectories and position histograms 629
did not differ significantly between the two animals, indicating 630
that the hydrogel implants do not adversely impact animal 631
health (Figure 6b–f). During times of stress or infections, the 632
fish may swim violently or erratically. In the case of serious 633
illness, fish movement would slow severely.^{76,77} The video data 634
and position histograms (Figure 6c–f) show that the subject fish 635
showed neither erratic movement nor stationary behavior 636
relative to the control. The absence of other abnormalities, 637
such as damaged fins, disinterest in food, and discoloration, 638
further indicate that the fish tolerated the implant well.⁷⁸ 639

640 Furthermore, goldfish were maintained up to six months with
641 the hydrogel implant, indicating long-term biocompatibility.

642 These results effectively form a pilot study that can be used to
643 direct and prioritize future work involving larger sample sizes, a
644 greater diversity of species, optimization of the hydrogel and
645 delivery method, and development of a wearable fluorescence
646 reader.

647 ■ CONCLUSIONS

648 In summary, the feasibility of applying CoPhMoRe sensors for
649 the physiological biologging of marine organisms was
650 demonstrated in nine species of aquatic vertebrates. Future
651 work will perform similar tissue penetration, tissue hetero-
652 geneity, and biocompatibility studies with a larger number of
653 animals to probe phenotypic diversity. Strategies to normalize
654 sensor signals against individual implant site optical properties
655 and internal fluorescent standards will be explored to create
656 absolute interspecies calibrations. Ratiometric approaches to
657 optical sensing will mitigate movement and other artifacts that
658 may confound the signal.⁴⁴ The successful measurement of the
659 fluorescent hydrogels using an inexpensive, field portable
660 Raspberry Pi imaging setup motivates further efforts to design
661 a wearable, flexible sensor tag that integrates optoelectronic
662 components tailored for physiological biologging using SWNT-
663 gels. These technical improvements may improve the signal-to-
664 noise ratio, time resolution of the measurements, and stability of
665 the signal when attached to a moving animal. In parallel, the
666 underlying SWNT nanosensors may be engineered to be
667 sensitive to a wider range of bioanalytes to investigate a wider
668 range of physiological states. The detection range of the
669 riboflavin sensor described herein will be further improved to be
670 sensitive to the physiologically relevant range. This work
671 advances the application of biosensors into animals beyond
672 the commonly used rodent and zebrafish models and carves a
673 path toward the physiological biologging of aquatic organisms.

674 ■ ASSOCIATED CONTENT

675 ⓘ Supporting Information

676 The Supporting Information is available free of charge on the
677 ACS Publications website at DOI: 10.1021/acssens-
678 sors.8b00538.

679 Fit parameters for optical penetration depth model,
680 comparison of SWNT fluorescence and photoresponsiv-
681 ity of common photodetectors (PDF)

682 ■ AUTHOR INFORMATION

683 Corresponding Author

684 *E-mail: strano@mit.edu.

685 ORCID

686 Michael S. Strano: 0000-0003-2944-808X

687 Notes

688 The authors declare no competing financial interest.

689 ■ ACKNOWLEDGMENTS

690 This research was supported by the King Abdullah University of
691 Science & Technology (OSR-2015 Sensors 2707). FTN is
692 supported by the Arnold and Mabel Beckman Foundation
693 through the Arnold O. Beckman Postdoctoral Fellowship. The
694 authors are also grateful to the Oceanographic animal care staff for
695 performing histological analysis, helpful discussions, and
696 financial support (OCE-10-18) in performing this research.

We also thank the Health and Animal Pathology Group, Dpt. 697
PASAPTA, Facultad de Veterinaria, Universidad Cardenal 698
Herrera-CEU, CEU Universities, for performing histological 699
analysis and interpretation. 700

701 ■ ABBREVIATIONS

SWNT, single wall carbon nanotube; CoPhMoRe, corona phase 702
molecular recognition; nIR, near-infrared; PEGDA, poly- 703
(ethylene glycol) diacrylate; ss(AC)₁₅, single-stranded (AC)₁₅ 704
DNA; InGaAs, Indium gallium arsenide 705

706 ■ REFERENCES

- (1) McIntyre, T. Trends in Tagging of Marine Mammals: A Review of 707
Marine Mammal Biologging Studies. *African J. Mar. Sci.* **2014**, *36* (4), 708
409–422. 709
- (2) Cooke, S. J.; Brownscombe, J. W.; Raby, G. D.; Broell, F.; Hinch, S. 710
G.; Clark, T. D.; Semmens, J. M. Remote Bioenergetics Measurements 711
in Wild Fish: Opportunities and Challenges. *Comp. Biochem. Physiol.,* 712
Part A: Mol. Integr. Physiol. **2016**, *202*, 23–37. 713
- (3) Watanabe, Y. Y.; Ito, M.; Takahashi, A. Testing Optimal Foraging 714
Theory in a Penguin–krill System. *Proc. R. Soc. London, Ser. B* **2014**, *281* 715
(1779), 20132376. 716
- (4) Amélineau, F.; Fort, J.; Mathewson, P. D.; Speirs, D. C.; Courbin, 717
N.; Perret, S.; Porter, W. P.; Wilson, R. J.; Grémillet, D. Energyscapes 718
and Prey Fields Shape a North Atlantic Seabird Wintering Hotspot 719
under Climate Change. *R. Soc. Open Sci.* **2018**, *5*, 171883. 720
- (5) Barnett, A.; Payne, N. L.; Semmens, J. M.; Fitzpatrick, R. 721
Ecotourism Increases the Field Metabolic Rate of Whitetip Reef Sharks. 722
Biol. Conserv. **2016**, *199*, 132–136. 723
- (6) Baylis, A. M.M.; Orben, R. A.; Arnould, J. P.Y.; Peters, K.; Knox, 724
T.; Costa, D. P.; Staniland, I. J. Diving Deeper into Individual Foraging 725
Specializations of a Large Marine Predator, the Southern Sea Lion. 726
Oecologia **2015**, *179* (4), 1053–1065. 727
- (7) Hays, G. C.; Scott, R. Global Patterns for Upper Ceilings on 728
Migration Distance in Sea Turtles and Comparisons with Fish, Birds 729
and Mammals. *Funct. Ecol.* **2013**, *27* (3), 748–756. 730
- (8) Yasuda, T.; Kawabe, R.; Takahashi, T.; Murata, H.; Kurita, Y.; 731
Nakatsuka, N.; Arai, N. Habitat Shifts in Relation to the Reproduction 732
of Japanese Flounder *Paralichthys Olivaceus* Revealed by a Depth- 733
Temperature Data Logger. *J. Exp. Mar. Biol. Ecol.* **2010**, *385* (1–2), 50– 734
58. 735
- (9) Zhang, J.; Landry, M. P.; Barone, P. W.; Kim, J.-H.; Lin, S.; Ulissi, 736
Z. W.; Lin, D.; Mu, B.; Boghossian, A. A.; Hilmer, A. J.; et al. Molecular 737
Recognition Using Corona Phase Complexes Made of Synthetic 738
Polymers Adsorbed on Carbon Nanotubes. *Nat. Nanotechnol.* **2013**, *8* 739
(12), 959–968. 740
- (10) Wu, D.; Sedgwick, A. C.; Gunnlaugsson, T.; Akkaya, E. U.; Yoon, 741
J.; James, T. D. Fluorescent Chemosensors: The Past, Present and 742
Future. *Chem. Soc. Rev.* **2017**, *46* (23), 7105–7123. 743
- (11) Xiao, T.; Wu, F.; Hao, J.; Zhang, M.; Yu, P.; Mao, L. In Vivo 744
Analysis with Electrochemical Sensors and Biosensors. *Anal. Chem.* 745
2017, *89* (1), 300–313. 746
- (12) Sun, W.; Guo, S.; Hu, C.; Fan, J.; Peng, X. Recent Development 747
of Chemosensors Based on Cyanine Platforms. *Chem. Rev.* **2016**, *116* 748
(14), 7768–7817. 749
- (13) Soto, R. J.; Hall, J. R.; Brown, M. D.; Taylor, J. B.; Schoenfish, M. 750
H. In Vivo Chemical Sensors: Role of Biocompatibility on Performance 751
and Utility. *Anal. Chem.* **2017**, *89* (1), 276–299. 752
- (14) Rong, G.; Corrie, S. R.; Clark, H. A. In Vivo Biosensing: Progress 753
and Perspectives. *ACS Sensors* **2017**, *2* (3), 327–338. 754
- (15) Howes, P. D.; Chandrawati, R.; Stevens, M. M. Colloidal 755
Nanoparticles as Advanced Biological Sensors. *Science (Washington,* 756
DC, U. S.) **2014**, *346* (6205), 1247390. 757
- (16) Carter, K. P.; Young, A. M.; Palmer, A. E. Fluorescent Sensors for 758
Measuring Metal Ions in Living Systems. *Chem. Rev.* **2014**, *114* (8), 759
4564–4601. 760

- (17) Scholten, K.; Meng, E. A Review of Implantable Biosensors for Closed-Loop Glucose Control and Other Drug Delivery Applications. *Int. J. Pharm.* **2018**, *544* (2), 319–334.
- (18) Cotruvo, J. A., Jr.; Aron, A. T.; Ramos-Torres, K. M.; Chang, C. J. Synthetic Fluorescent Probes for Studying Copper in Biological Systems. *Chem. Soc. Rev.* **2015**, *44* (13), 4400–4414.
- (19) Sun, K.; Yang, Y.; Zhou, H.; Yin, S.; Qin, W.; Yu, J.; Chiu, D. T.; Yuan, Z.; Zhang, X.; Wu, C. Ultrabright Polymer-Dot Transducer Enabled Wireless Glucose Monitoring via a Smartphone. *ACS Nano* **2018**, *12* (6), 5176–5184.
- (20) Deng, B.; Ren, M.; Kong, X.; Zhou, K.; Lin, W. Development of an Enhanced Turn-on Fluorescent HOCl Probe with a Large Stokes Shift and Its Use for Imaging HOCl in Cells and Zebrafish. *Sens. Actuators, B* **2018**, *255*, 963–969.
- (21) Gurkov, A.; Sadvoy, A.; Shchapova, E.; Teh, C.; Meglinski, I.; Timofeyev, M. Microencapsulated Fluorescent PH Probe as Implantable Sensor for Monitoring the Physiological State of Fish Embryos. *PLoS One* **2017**, *12* (10), e0186548.
- (22) Ferreira, N. R.; Ledo, A.; Laranjinha, J.; Gerhardt, G. A.; Barbosa, R. M. Simultaneous Measurements of Ascorbate and Glutamate in Vivo in the Rat Brain Using Carbon Fiber Nanocomposite Sensors and Microbiosensor Arrays. *Bioelectrochemistry* **2018**, *121*, 142–150.
- (23) Mehrotra, P. Biosensors and Their Applications - A Review. *J. Oral Biol. Craniofacial Res.* **2016**, *6* (2), 153–159.
- (24) Bisker, G.; Dong, J.; Park, H. D.; Iverson, N. M.; Ahn, J.; Nelson, J. T.; Landry, M. P.; Kruss, S.; Strano, M. S. Protein-Targeted Corona Phase Molecular Recognition. *Nat. Commun.* **2016**, *7*, 10241.
- (25) Zhang, J. Q.; Boghossian, A. A.; Barone, P. W.; Rwei, A.; Kim, J. H.; Lin, D. H.; Heller, D. A.; Hilmer, A. J.; Nair, N.; Reuel, N. F.; et al. Single Molecule Detection of Nitric Oxide Enabled by d(AT)(15) DNA Adsorbed to Near Infrared Fluorescent Single-Walled Carbon Nanotubes. *J. Am. Chem. Soc.* **2011**, *133* (3), 567–581.
- (26) Jin, H.; Heller, D. A.; Kalbacova, M.; Kim, J.-H.; Zhang, J.; Boghossian, A. A.; Maheshri, N.; Strano, M. S. Detection of Single-Molecule H₂O₂ Signaling from Epidermal Growth Factor Receptor Using Fluorescent Single-Walled Carbon Nanotubes. *Nat. Nanotechnol.* **2010**, *5* (4), 302–309.
- (27) Kruss, S.; Landry, M. P.; Vander Ende, E.; Lima, B. M. A.; Reuel, N. F.; Zhang, J.; Nelson, J.; Mu, B.; Hilmer, A.; Strano, M. Neurotransmitter Detection Using Corona Phase Molecular Recognition on Fluorescent Single-Walled Carbon Nanotube Sensors. *J. Am. Chem. Soc.* **2014**, *136* (2), 713–724.
- (28) Kruss, S.; Salem, D. P.; Vuković, L.; Lima, B.; Vander Ende, E.; Boyden, E. S.; Strano, M. S. High-Resolution Imaging of Cellular Dopamine Efflux Using a Fluorescent Nanosensor Array. *Proc. Natl. Acad. Sci. U. S. A.* **2017**, *114* (8), 1789–1794.
- (29) Bisker, G.; Bakh, N. A.; Lee, M. A.; Ahn, J.; Park, M.; O’Connell, E. B.; Iverson, N. M.; Strano, M. S. Insulin Detection Using a Corona Phase Molecular Recognition Site on Single-Walled Carbon Nanotubes. *ACS Sensors* **2018**, *3* (2), 367–377.
- (30) Iverson, N. M.; Barone, P. W.; Shandell, M.; Trudel, L. J.; Sen, S.; Sen, F.; Ivanov, V.; Atolia, E.; Farias, E.; McNicholas, T. P.; et al. In Vivo Biosensing via Tissue-Localizable near-Infrared-Fluorescent Single-Walled Carbon Nanotubes. *Nat. Nanotechnol.* **2013**, *8* (11), 873–880.
- (31) Hays, G. C.; Ferreira, L. C.; Sequeira, A. M. M.; Meekan, M. G.; Duarte, C. M.; Bailey, H.; Bailleul, F.; Bowen, W. D.; Caley, M. J.; Costa, D. P.; et al. Key Questions in Marine Megafauna Movement Ecology. *Trends Ecol. Evol.* **2016**, *31* (6), 463–475.
- (32) Payne, N. L.; Taylor, M. D.; Watanabe, Y. Y.; Semmens, J. M. From Physiology to Physics: Are We Recognizing the Flexibility of Biologging Tools? *J. Exp. Biol.* **2014**, *217* (3), 317–322.
- (33) Wilson, R. P.; Gómez-Laich, A.; Sala, J. E.; Dell’Omo, G.; Holton, M. D.; Quintana, F. Long Necks Enhance and Constrain Foraging Capacity in Aquatic Vertebrates. *Proc. R. Soc. London, Ser. B* **2017**, *284* (1867), 20172072.
- (34) Meekan, M. G.; Fuiman, L. A.; Davis, R.; Berger, Y.; Thums, M. Swimming Strategy and Body Plan of the World’s Largest Fish: Implications for Foraging Efficiency and Thermoregulation. *Front. Mar. Sci.* **2015**, *2*, 64.
- (35) Lee, M. A.; Bakh, N.; Bisker, G.; Brown, E. N.; Strano, M. S. A Pharmacokinetic Model of a Tissue Implantable Cortisol Sensor. *Adv. Healthcare Mater.* **2016**, *5* (23), 3004–3015.
- (36) Pon, L. B.; Hinch, S. G.; Cooke, S. J.; Patterson, D. A.; Farrell, A. P. Physiological, Energetic and Behavioural Correlates of Successful Fishway Passage of Adult Sockeye Salmon *Oncorhynchus Nerka* in the Seton River, British Columbia. *J. Fish Biol.* **2009**, *74* (6), 1323–1336.
- (37) Crossin, G. T.; Takahashi, A.; Sakamoto, K. Q.; Trathan, P. N.; Williams, T. D. Habitat Selection by Foraging Macaroni Penguins Correlates with Hematocrit, an Index of Aerobic Condition. *Mar. Ecol. Prog. Ser.* **2015**, *530*, 163–176.
- (38) O’Toole, A. C.; Dechraoui Bottein, M. Y.; Danylchuk, A. J.; Ramsdell, J. S.; Cooke, S. J. Linking Ciguatera Poisoning to Spatial Ecology of Fish: A Novel Approach to Examining the Distribution of Biotxin Levels in the Great Barracuda by Combining Non-Lethal Blood Sampling and Biotelemetry. *Sci. Total Environ.* **2012**, *427–428*, 98–105.
- (39) Kruss, S.; Hilmer, A. J.; Zhang, J.; Reuel, N. F.; Mu, B.; Strano, M. S. Carbon Nanotubes as Optical Biomedical Sensors. *Adv. Drug Delivery Rev.* **2013**, *65* (15), 1933–1950.
- (40) Bisker, G.; Iverson, N. M.; Ahn, J.; Strano, M. S. A Pharmacokinetic Model of a Tissue Implantable Insulin Sensor. *Adv. Healthcare Mater.* **2015**, *4* (1), 87–97.
- (41) Massey, V. The Chemical and Biological Versatility of Riboflavin. *Biochem. Soc. Trans.* **2000**, *28* (4), 283–296.
- (42) Nakashima, N.; Okuzono, S.; Murakami, H.; Nakai, T.; Yoshikawa, K. DNA Dissolves Single-Walled Carbon Nanotubes in Water. *Chem. Lett.* **2003**, *32* (5), 456–457.
- (43) Zheng, M.; Jagota, A.; Semke, E. D.; Diner, B. A.; McLean, R. S.; Lustig, S. R.; Richardson, R. E.; Tassi, N. G. DNA-Assisted Dispersion and Separation of Carbon Nanotubes. *Nat. Mater.* **2003**, *2* (5), 338–342.
- (44) Giraldo, J. P.; Landry, M. P.; Kwak, S. Y.; Jain, R. M.; Wong, M. H.; Iverson, N. M.; Ben-Naim, M.; Strano, M. S. A Ratiometric Sensor Using Single Chirality Near-Infrared Fluorescent Carbon Nanotubes: Application to in Vivo Monitoring. *Small* **2015**, *11* (32), 3973–3984.
- (45) Zhang, J.; Kruss, S.; Hilmer, A. J.; Shimizu, S.; Schmois, Z.; De La Cruz, F.; Barone, P. W.; Reuel, N. F.; Heller, D. A.; Strano, M. S. A Rapid, Direct, Quantitative, and Label-Free Detector of Cardiac Biomarker Troponin T Using Near-Infrared Fluorescent Single-Walled Carbon Nanotube Sensors. *Adv. Healthcare Mater.* **2014**, *3* (3), 412–423.
- (46) Larsen, B. A.; Deria, P.; Holt, J. M.; Stanton, I. N.; Heben, M. J.; Therien, M. J.; Blackburn, J. L. Effect of Solvent Polarity and Electrophilicity on Quantum Yields and Solvatochromic Shifts of Single-Walled Carbon Nanotube Photoluminescence. *J. Am. Chem. Soc.* **2012**, *134* (30), 12485–12491.
- (47) Choi, J. H.; Strano, M. S. Solvatochromism in Single-Walled Carbon Nanotubes. *Appl. Phys. Lett.* **2007**, *90* (22), 88–91.
- (48) Tokarev, I.; Minko, S. Stimuli-Responsive Porous Hydrogels at Interfaces for Molecular Filtration, Separation, Controlled Release, and Gating in Capsules and Membranes. *Adv. Mater.* **2010**, *22* (31), 3446–3462.
- (49) Zhao, F.; Yao, D.; Guo, R.; Deng, L.; Dong, A.; Zhang, J. Composites of Polymer Hydrogels and Nanoparticulate Systems for Biomedical and Pharmaceutical Applications. *Nanomaterials* **2015**, *5* (4), 2054–2130.
- (50) Peppas, N. A.; Huang, Y.; Torres-Lugo, M.; Ward, J. H.; Zhang, J. Physicochemical Foundations and Structural Design of Hydrogels in Medicine and Biology. *Annu. Rev. Biomed. Eng.* **2000**, *2* (1), 9–29.
- (51) Peppas, N. A.; Hilt, J. Z.; Khademhosseini, A.; Langer, R. Hydrogels in Biology and Medicine: From Molecular Principles to Bionanotechnology. *Adv. Mater.* **2006**, *18* (11), 1345–1360.
- (52) Pedersen, J. S.; Sommer, C. Temperature Dependence of the Virial Coefficients and the Chi Parameter in Semi-Dilute Solutions of PEG. *Prog. Colloid Polym. Sci.* **2005**, *130*, 70–78.
- (53) Hays, G. C.; Bastian, T.; Doyle, T. K.; Fossette, S.; Gleiss, A. C.; Gravenor, M. B.; Hobson, V. J.; Humphries, N. E.; Lilley, M. K. S.; Pade, N. G.; et al. High Activity and Levy Searches: Jellyfish Can Search the

- 899 Water Column like Fish. *Proc. R. Soc. London, Ser. B* **2012**, *279* (1728),
900 465–473.
- 901 (54) Göröcs, Z.; Rivenson, Y.; Ceylan Koydemir, H.; Tseng, D.; Troy,
902 T. L.; Demas, V.; Ozcan, A. Quantitative Fluorescence Sensing
903 Through Highly Autofluorescent, Scattering, and Absorbing Media
904 Using Mobile Microscopy. *ACS Nano* **2016**, *10* (9), 8989–8999.
- 905 (55) Lim, C.; Leamaster, B.; Brock, J. A. Riboflavin Requirement of
906 Fingerling Red Hybrid Tilapia Grown in Seawater. *J. World Aquacult.*
907 *Soc.* **1993**, *24* (4), 451–458.
- 908 (56) Petteys, B. J.; Frank, E. L. Rapid Determination of Vitamin B2
909 (Riboflavin) in Plasma by HPLC. *Clin. Chim. Acta* **2011**, *412* (1), 38–
910 43.
- 911 (57) Yao, Y.; Yonezawa, A.; Yoshimatsu, H.; Omura, T.; Masuda, S.;
912 Matsubara, K. Involvement of Riboflavin Transporter RFVT2/Slc52a2
913 in Hepatic Homeostasis of Riboflavin in Mice. *Eur. J. Pharmacol.* **2013**,
914 *714* (1), 281–287.
- 915 (58) Bashkatov, A. N.; Genina, E. A.; Kochubey, V. I.; Tuchin, V. V.
916 Optical Properties of Human Skin, Subcutaneous and Mucous Tissues
917 in the Wavelength Range from 400 to 2000 Nm. *J. Phys. D: Appl. Phys.*
918 **2005**, *38* (15), 2543–2555.
- 919 (59) Smith, A. M.; Mancini, M. C.; Nie, S. Bioimaging: Second
920 Window for in Vivo Imaging. *Nat. Nanotechnol.* **2009**, *4*, 710–711.
- 921 (60) Welscher, K.; Liu, Z.; Sherlock, S. P.; Robinson, J. T.; Chen, Z.;
922 Daranciang, D.; Dai, H. A Route to Brightly Fluorescent Carbon
923 Nanotubes for Near-Infrared Imaging in Mice. *Nat. Nanotechnol.* **2009**,
924 *4* (11), 773–780.
- 925 (61) Luo, S.; Zhang, E.; Su, Y.; Cheng, T.; Shi, C. A Review of NIR
926 Dyes in Cancer Targeting and Imaging. *Biomaterials* **2011**, *32* (29),
927 7127–7138.
- 928 (62) Iverson, N. M.; Bisker, G.; Farias, E.; Ivanov, V.; Ahn, J.; Wogan,
929 G. N.; Strano, M. S. Quantitative Tissue Spectroscopy of near Infrared
930 Fluorescent Nanosensor Implants. *J. Biomed. Nanotechnol.* **2016**, *12*
931 (5), 1035–1047.
- 932 (63) Hawkes, J. W. The Structure of Fish Skin. *Cell Tissue Res.* **1974**,
933 *149* (713), 147–158.
- 934 (64) Jordan, T. M.; Partridge, J. C.; Roberts, N. W. Non-Polarizing
935 Broadband Multilayer Reflectors in Fish. *Nat. Photonics* **2012**, *6* (11),
936 759–763.
- 937 (65) Spotila, J. R. *Sea Turtles: A Complete Guide to Their Biology,*
938 *Behavior, and Conservation*; Johns Hopkins University Press: Baltimore,
939 2004.
- 940 (66) Ng, K.-C. C.; Ooi, A.-C. P. A Review of Fish Taxonomy
941 Conventions and Species Identification Techniques. *J. Surv. Fish. Sci.*
942 **2017**, *4* (1), 54–93.
- 943 (67) Human, B. A.; Owen, E. P.; Compagno, L. J. V.; Harley, E. H.
944 Testing Morphologically Based Phylogenetic Theories within the
945 Cartilaginous Fishes with Molecular Data, with Special Reference to the
946 Catshark Family (Chondrichthyes; Scyliorhinidae) and the Interrela-
947 tionships within Them. *Mol. Phylogenet. Evol.* **2006**, *39* (2), 384–391.
- 948 (68) Kosoglu, M. A.; Hood, R. L.; Chen, Y.; Xu, Y.; Rylander, M. N.;
949 Rylander, C. G. Fiber Optic Microneedles for Transdermal Light
950 Delivery: Ex Vivo Porcine Skin Penetration Experiments. *J. Biomech.*
951 *Eng.* **2010**, *132* (9), 91014–91017.
- 952 (69) Matzeu, G.; Florea, L.; Diamond, D. Advances in Wearable
953 Chemical Sensor Design for Monitoring Biological Fluids. *Sens.*
954 *Actuators, B* **2015**, *211*, 403–418.
- 955 (70) Allaby, M. Carcharhinidae. In *A Dictionary of Zoology*; Oxford
956 University Press, 2009.
- 957 (71) Jacques, S. L. Optical Properties of Biological Tissues: A Review.
958 *Phys. Med. Biol.* **2013**, *58* (11), R37–R61.
- 959 (72) Anderson, R. R.; Parrish, J. A. The Optics of Human Skin. *J.*
960 *Invest. Dermatol.* **1981**, *77* (1), 13–19.
- 961 (73) Nassar, J. M.; Khan, S. M.; Velling, S. J.; Diaz-Gaxiola, A.; Shaikh,
962 S. F.; Gerald, N. R.; Torres Sevilla, G. A.; Duarte, C. M.; Hussain, M.
963 M. Compliant Lightweight Non-Invasive Standalone “Marine Skin”
964 Tagging System. *npj Flex. Electron.* **2018**, *2* (1), 13.
- 965 (74) Ando, A.; Hatori, M.; Hagiwara, Y.; Isefuku, S.; Itoi, E. Imaging
966 Features of Foreign Body Granuloma in the Lower Extremities
Mimicking a Soft Tissue Neoplasm. *Upsala J. Med. Sci.* **2009**, *114* (1), 967
46–51. 968
- (75) Anderson, J. M.; Rodriguez, A.; Chang, D. T. Foreign Body 969
Reaction to Biomaterials. *Semin. Immunol.* **2008**, *20* (2), 86–100. 970
- (76) Adelman, J. S.; Martin, L. B. Vertebrate Sickness Behaviors: 971
Adaptive and Integrated Neuroendocrine Immune Responses. *Integr.* 972
Comp. Biol. **2009**, *49* (3), 202–214. 973
- (77) Ashley, P. J.; Sneddon, L. U. Pain and Fear in Fish. In *Fish* 974
Welfare; Branson, E. J., Ed.; Blackwell, 2008; 49–77. 975
- (78) Stoskopf, M. K. Biology and Management of Laboratory Fishes. 976
In *Laboratory Animal Medicine*, Anderson, L. C.; Otto, G. M.; Pritchett- 977
Corning, K. R.; Whary, M. T. B. T., Eds.; Academic Press: Boston, 978
2015; pp 1063–1086. 979